1 **Chemical-genetic interaction mapping links carbon metabolism and cell wall**

2 **structure to tuberculosis drug efficacy**

3

4 Eun-Ik Koh[1], Nadine Ruecker[2], Megan K. Proulx[1], Vijay Soni[2], Kenan C. Murphy[1],

5 Kadamba G. Papavinasasundaram[1], Charlotte J. Reames[1], Carolina Trujillo[2], Anisha

6 Zaveri[2], Matthew D. Zimmerman[3], Roshanak Aslebagh[4,5], Richard E. Baker[1], Scott A.

7 Shaffer[4,5], Kristine M. Guinn[6], Michael Fitzgerald[7], Véronique A. Dartois[3,8], Sabine Ehrt[2],

8 Deborah T. Hung[7,9,10], Thomas R. Ioerger[11], Eric Rubin[6], Kyu Y. Rhee[2], Dirk

9 Schnappinger[2] and Christopher M. Sassetti[1]

10

11 [1] Department of Microbiology and Physiological Systems, University of Massachusetts

12 Medical School, Worcester, Massachusetts, 01655 USA

13 [2] Department of Microbiology and Immunology, Weill Cornell Medical College, New

14 York, New York, 10065 USA

15 [3] Center for Discovery and Innovation, Hackensack Meridian Health, Nutley, New

16 Jersey, 07110 USA

17 [4] Department of Biochemistry and Molecular Pharmacology, University of

18 Massachusetts Medical School, Worcester, Massachusetts, 01655 USA

19 [5] Mass Spectrometry Facility, University of Massachusetts Medical School, Shrewsbury,

20 Massachusetts, 01545 USA

21 [6] Department of Immunology and Infectious Diseases, Harvard T.H. Chan School of

22 Public Health, Boston, Massachusetts, 02115 USA

23 [7] Broad Institute of MIT and Harvard, Cambridge, Massachusetts, 02142 USA

24   [8] Department of Medical Sciences, Hackensack School of Medicine, Nutley, New

25   Jersey, 07110 USA

26   [9] Department of Molecular Biology and Center for Computation and Integrative Biology,

27   Massachusetts General Hospital, Boston, Massachusetts, 02114 USA

28   [10] Department of Genetics, Harvard Medical School, Boston, Massachusetts, 02114

29   USA

30   [11] Department of Computer Science and Engineering, Texas A&M University, College

31   Station, Texas, 77840 USA

32

33   Corresponding author:

34   Christopher M. Sassetti

35   368 Plantation Street, AS8-2051, Worcester, MA 01605

36   508-856-3678

37   Christopher.sassetti@umassmed.edu

38

Abstract

Current chemotherapy against *Mycobacterium tuberculosis (Mtb)*, an important human pathogen, requires a multidrug regimen lasting several months. While efforts have been made to optimize therapy by exploiting drug-drug synergies, testing new drug combinations in relevant host environments remains arduous. In particular, host environments profoundly affect the bacterial metabolic state and drug efficacy, limiting the accuracy of predictions based on *in vitro* assays alone. In this study, we utilize conditional *Mtb* knockdown mutants of essential genes as an experimentally-tractable surrogate for drug treatment, and probe the relationship between *Mtb* carbon metabolism and chemical-genetic interactions (CGI). We examined the anti-tubercular drugs isoniazid, rifampicin and moxifloxacin, and found that CGI are differentially responsive to the metabolic state, defining both environment-independent and –dependent synergies. Specifically, growth on the *in vivo*-relevant carbon source, cholesterol, reduced rifampicin efficacy by altering mycobacterial cell surface lipid composition. We report that a variety of perturbations in cell wall synthesis pathways restore rifampicin efficacy during growth on cholesterol, and that both environment-independent and cholesterol-dependent *in vitro* CGI could be leveraged to enhance bacterial clearance in the mouse infection model. Our findings present an atlas of novel chemical-genetic-environmental synergies that can be used to optimize drug-drug interactions as well as provide a framework for understanding *in vitro* correlates of *in vivo* efficacy.

62 **Significance**

63 Efforts to improve tuberculosis therapy include optimizing multi-drug regimens to take

64 advantage of drug-drug synergies. However, the complex host environment has a

65 profound effect on bacterial metabolic state and drug activity, making predictions of

66 optimal drug combinations difficult. In this study, we leverage a newly developed library

67 of conditional knockdown *Mycobacterium tuberculosis* mutants in which genetic

68 depletion of essential genes mimics the effect of drug therapy. This tractable system

69 allowed us to assess the effect of growth condition on predicted drug-drug interactions.

70 We found that these interactions can be differentially sensitive to the metabolic state

71 and select *in vitro*-defined synergies can be leveraged to accelerate bacterial killing

72 during infection. These findings suggest new strategies for optimizing tuberculosis

73 therapy.

74

75

76 **Introduction**

77 The current chemotherapeutic regimen for tuberculosis (TB) is the product of many

78 decades of basic and clinical research. Since the first trials of streptomycin

79 monotherapy in 1948 were rapidly followed by the emergence of antibiotic resistant

80 clones (1), multidrug regimens to both suppress resistance and accelerate bacterial

81 killing have become standard. The current regimen used against drug-sensitive strains

82 of *Mycobacterium tuberculosis* (*Mtb*) consists of four antibiotics, isoniazid (INH),

83 rifampicin (RIF), pyrazinamide (PZA), and ethambutol (EMB), and was optimized in a

84 series of clinical trials in the 1970s (2, 3). While this "short-course regimen" has been

85 credited with curing over 50 million patients, its delivery is complicated by the need for

86 6-9 months of drug administration (4). Furthermore, even in clinical trial settings where

87 the delivery of this extended regimen is assured, 5-10% of patients fail therapy (5). The

88 frequent transmission of antibiotic resistant *Mtb* strains has further complicated TB

89 treatment options, requiring the use of less optimized drug combinations that are

90 administered for even longer periods (6).

91

92 The factors that necessitate prolonged therapy are complex and specific to the infection

93 environment. While antibiotics such as INH and RIF cause rapid cell death *in vitro*, their

94 antimicrobial activities are much slower during infection (7). Limited drug penetration

95 into *Mtb*-containing tissue lesions may reduce the efficacy of some drugs. For example,

96 the intralesional RIF concentrations are significantly lower than what is achieved in the

97 plasma (8, 9), and clinical studies suggest that increased RIF dosing improves bacterial

98 clearance (10, 11). However, drug penetration is unlikely to fully account for the reduced

99   antibiotic efficacy in host tissue, as this complex and stressful environment has also

100   been shown to alter the physiology of the pathogen to induce a drug-tolerant state (12–

101   14). While a number of host immune-related stresses may be involved in this process,

102   simple changes in macronutrient availability can have important consequences. *Mtb* has

103   access to a mixture of glycolytic carbon sources, fatty acids and cholesterol in host

104   tissue (15–17), and altering the availability of these carbon sources *in vitro* can change

105   the efficacy of anti-tubercular compounds (18–23). A role for differential carbon

106   catabolism in determining drug efficacy is also supported by the identification of natural

107   genetic variants in clinical *Mtb* isolates that enhance drug tolerance by altering either

108   glycerol, lipid, or sterol catabolism (24, 25). The profound effect of the host environment

109   on bacterial metabolic state and drug activity makes it difficult to predict the ultimate

110   efficacy of an antibiotic regimen based on *in vitro* assays alone.

111

112   The most advanced efforts to accelerate TB therapy involve optimizing multi-drug

113   regimens to take advantage of drug-drug synergies. These pharmacological

114   interactions can improve therapy by increasing drug exposure, decreasing MIC, or

115   enhancing the maximal effect of the treatment (26). However, despite the demonstrated

116   benefits of synergistic regimens in many therapeutic realms, the combinatorial burden of

117   testing all potential multi-drug combinations remains cumbersome. While recent

118   advances to more efficiently predict synergies *in vitro* have proven valuable (27, 28), it

119   remains unclear whether the environmental influences that so profoundly alter the

120   efficacy of individual drugs will also influence drug-drug interactions (29, 30).

121

122   In this study, we leveraged a newly developed genetic resource to understand the effect

123   of growth conditions on potential drug-drug synergies. This "hypomorph library" consists

124   of individually DNA barcoded strains in which individual essential genes are tagged with

125   the DAS+4 sequence that targets proteins for degradation upon inducible induction of

126   the SspB adapter (31). Graded *sspB* expression produces different degrees of depletion

127   to model the effect of partial chemical inhibition (32). This approach allowed for highly

128   parallel assessment of chemical-genetic interactions (CGI) between individual

129   hypomorphic alleles and TB drugs under different growth conditions. We report that

130   drugs of distinct classes produce synergies that are differentially sensitive to the

131   environment, and that both condition-independent and –dependent CGIs can be

132   identified for all drugs tested. In particular, RIF efficacy was impaired as a result of cell

133   surface lipid alterations that occur during growth in cholesterol, and the cell could be

134   resensitized through a condition-specific interaction with the cell wall synthetic

135   machinery both *in vitro* and in the mouse lung. These observations provide a

136   compendium of chemical-genetic synergies that can be exploited to enhance therapy

137   and begin to define *in vitro* correlates of *in vivo* efficacy.

138

139   **Results**

140   **Genetic strategy to define essential bacterial functions that alter drug efficacy *in***

141   ***vitro.***

142   Host environmental factors alter antibiotic efficacy against TB (12, 24, 33, 34). To

143   determine if carbon source availability specifically affects antibiotic efficacy, we used the

144   *Mtb* strain H37Rv in minimal medium with glycerol, acetate or cholesterol as sole

145   carbon sources in a growth inhibition assay with the TB drugs isoniazid (INH), rifampicin

146   (RIF) and moxifloxacin (MOX). As these carbon sources support different growth rates,

147   endpoint-based antibiotic activity measurements such as MIC assays can be difficult to

148   interpret. Therefore we quantified growth rates in each carbon source over multiple

149   concentrations of antibiotics to determine the concentration that decreased the growth

150   rate by 50% (GR_{50}) (24, 35). We found different carbon sources to alter the GR_{50} of

151   these drugs in distinct ways. For INH, glycerol-dependent growth increased efficacy,

152   relative to the non-glycolytic carbon sources. In contrast, growth in cholesterol was

153   found to decrease RIF efficacy, relative to the other conditions. Media composition had

154   a more modest effect on MOX, altering GR_{50} by only approximately 2-fold **(Fig1A)**.

155   These findings show that carbon metabolism plays an important role in antibiotic

156   efficacy and has distinct effects on different drugs.

157

158   To understand the mechanisms linking drug efficacy and metabolism, we utilized a

159   barcoded-hypomorph library consisting of 465 essential genes to identify CGI with these

160   drugs (32). The library was grown in minimal media with glycerol, acetate or cholesterol,

161   and antibiotics were added at concentrations ranging from 0.05X to 1X GR_{50} for each.

162   Bacteria were subjected to these conditions in 96-well plates for 14 days, at which point

163   the relative abundance of individual mutants was assessed through multiplex PCR and

164   Next-Generation Sequencing **(Fig1B, S.Table 1)**. Relative abundances of individual

165   mutants were calculated by normalizing the mutant's barcode count to the total barcode

166   count and comparing the relative abundance of each mutant in different drug

167   concentrations with the untreated control samples.

168

169   We initially investigated the validity of this dataset by determining if genetic inhibition of

170   each drug's target produced the expected CGI with that compound in standard glycerol-

171   dependent growth conditions. RIF and MOX interact with the RNA polymerase subunit,

172   RpoB or the DNA gyrase subunit, GyrA, respectively. As expected, *rpoB* and *gyrA*

173   hypomorphic mutants were hypersensitive to RIF or MOX, and the CGI increased with

174   drug concentration **(Fig1C)**. The major target of INH, InhA, was not present in our

175   mutant pool. However, the library did contain a *ndh* mutant. Deficiency in this NADH-

176   dehydrogenase is known to decrease INH efficacy, likely due to the inefficient formation

177   of the active INH-NAD adduct (36). Consistent with these observations, we found that

178   the *ndh* hypomorphic mutant showed an INH dose-dependent increase in abundance in

179   our dataset **(Fig1C)**.

180

181   The hypomorph library was constructed to contain up to five different versions of each

182   DAS+4 tagged mutant, which express different levels of *sspB* and therefore produce

183   graded levels of protein depletion (31, 37). To investigate the relationship between

184   target protein abundance and phenotype, we correlated the strength of *sspB* expression

185   with drug sensitivity for a number of genes that were expected to alter antibiotic efficacy

186   **(Fig1D)**. For RIF, we concentrated on *rpoB*. For INH, we examined *ndh* as well as

187   genes associated with mycolate biosynthesis, and found *kasA* and *hadB* mutants to be

188   significantly hypersensitive to increasing INH concentrations. For MOX, in addition to

189   *gyrA*, depletion of proteins associated with DNA integrity or deoxynucleotide production,

190   *dnaN*, *lexA* and *ndrF2,* showed significantly decreased fitness over increasing MOX

191   concentrations. For some mutants, particularly those involved in DNA metabolism, we

192   noted a dose-dependent effect of *sspB* expression, with larger phenotypes

193   corresponding to greater degrees of depletion. However, this was not a universal

194   phenomenon, and we often found that independent mutants expressing different *sspB*

195   levels produced consistent phenotypic effects. The observed differences in sensitivity to

196   protein depletion likely reflect the unique biochemistry of each pathway (38). As a result,

197   we considered each mutant corresponding to a target protein independently in the

198   following analyses.

199

200   **CGI profiles are determined by the combination of carbon source and drug**

201   To understand the relative importance of carbon metabolism and drug on bacterial

202   physiology, we compared the "fitness profiles" of each condition, which represented the

203   relative fitness of each mutant strain. We first selected the fold change in abundance

204   (log2FC) values of every mutant at 0.65X GR_{50} drug concentration that showed a

205   statistically significant fitness difference when at least one treated sample was

206   compared to the untreated control (918 mutants, Q <0.05). 0.65X GR_{50} drug

207   concentration displayed the largest number of mutants with a statistically significant

208   fitness difference across most conditions. Upon hierarchical clustering of both genes

209   and conditions, we found three major condition clusters that corresponded to each

210   antibiotic **(Fig2A)**. These condition clusters were differentiated by two distinct clusters of

211   mutants; one large gene set differentiated MOX from the other drugs (Fig 2A bottom

212   cluster), and differential fitness effects on a second smaller gene set differentiated INH

213   and RIF (Fig2A top cluster). Within each condition cluster, fitness effects due to carbon

214   source were apparent.

215

216   To catalog the genes that differentiate these conditions, we compared each drug-

217   treated sample (0.65X GR_{50}) with the corresponding untreated control and chose genes

218   with log2FC < -1 and $p < 0.05$ for each carbon source. For all antibiotics tested, there

219   were genes that showed synergy across all carbon sources as well as those associated

220   with a single carbon source **(Fig2B)**. Notably, MOX produced the largest number of

221   synergies in a condition-independent manner, while INH and RIF produced the largest

222   number of synergies during acetate and cholesterol-dependent growth respectively. To

223   more quantitatively assess the relative contribution of carbon source and drug, we used

224   Principal Component Analysis (PCA) to examine the amount of variance contributed by

225   each, concentrating only on the INH and RIF conditions, which produced the most

226   condition-specific effects. PC1 aligned to distinguish the carbon sources, while PC2

227   differentiated among drug treatments **(Fig2C)**. The first and second principal

228   components accounted for 37.6% and 23.7% respectively, of the overall variance

229   across the 9 data sets, indicating that drug and carbon source played a relatively equal

230   role in shaping bacterial physiology.

231

232   **Condition-independent CGI can be reproduced with individual mutants.**

233   Genes found to alter antibiotic efficacy from the high-throughput hypomorph analysis

234   were validated using individual mutant strains. For initial validation studies, we

235   concentrated on mutants predicted to show drug-hypersensitivity under all media

236   conditions. The repression of a drug's target is thought to increase sensitivity to

237   inhibition by reducing the fraction of the target that needs to be inhibited to reduce

238   growth (39). As such, we anticipated that drug target inhibition would result in condition-

239   independent effects. This prediction was verified using a *rpoB* hypomorphic mutant,

240   which our screening data predicted to increase RIF efficacy in all carbon sources

241   **(Fig3A)**. When the MIC of RIF was determined using a standard microplate growth

242   assay, we verified that this degree of RpoB depletion decreased the RIF MIC by 4 to 16-

243   fold in each of the three media conditions **(Fig3A)**. In addition to known drug targets, a

244   number of additional genes were predicted to enhance RIF efficacy in a carbon source-

245   independent manner, including the transcriptional regulator, Rv0472c. This gene has

246   been named, mycolic acid desaturase regulator (*madR*), based on its specific effect on

247   the mycolate-modifying *desA1* and *desA2* genes (40). As we found for RpoB, MadR

248   depletion sensitized the bacterium to RIF in all tested carbon sources in the single strain

249   assay **(Fig3B)**. Finally, to ensure the specificity of these CGI, we investigated whether

250   they could be reversed by specific metabolite complementation. As predicted by the

251   screen, depletion of the lysine biosynthetic enzyme, LysA, produced RIF

252   hypersensitivity in both glycerol and cholesterol media, and we found this phenotype

253   was largely reversed by supplementation with 3mM lysine **(Fig3C)**. These data support

254   the predictions of the primary screen, and demonstrate that certain CGI are relatively

255   unaffected by carbon source.

256

257   **Depletion of cell-wall biosynthetic genes produces condition-specific RIF synergy**

258   As cholesterol represents a primary carbon source for *Mtb* during infection (16, 41), and

259   RIF efficacy is thought to be limited by drug exposure (42–44), we probed the

260   hypomorph fitness profiles for clues to the mechanism underlying the cholesterol-

261   dependent increase in RIF MIC. We found that inhibition of genes associated with

262   different components of the mycobacterial cell wall, including arabinogalactan (*embC*

263   and *aftB*), and mycolic acid (*kasA*) (45, 46) specifically sensitized the bacterium to RIF

264   during cholesterol growth **(Fig4A)**. These mutants were significantly underrepresented

265   by up to 8-fold upon RIF treatment specifically in cholesterol growth conditions across

266   multiple *sspB* doses and drug concentrations. To further explore the effect of cell wall

267   inhibition, we tested individual mutants with defects in peptidoglycan (*dapE*),

268   arabinogalactan (*aftB*), and mycolic acid (*hadB*) synthesis (45, 47–49). In this format,

269   we found that perturbation in each of these cell wall layers produced a similar effect, as

270   they all preferentially sensitized the bacterium to RIF in cholesterol growth conditions

271   **(Fig4BCD)**. These observations suggest that alterations in cell wall structure might

272   underlie the relationship between cholesterol catabolism and reduced RIF efficacy.

273

274   **RIF efficacy correlates with propionate catabolism and branched chain lipid**

275   **abundance.**

276   *Mtb* catabolizes cholesterol to pyruvate, propionyl-CoA and acetyl-CoA (17, 50).

277   Propionyl-CoA is a precursor of branched-chain lipid synthesis, and catabolism of either

278   cholesterol or propionate increases cellular propionyl-CoA levels causing an increase in

279   both the abundance and chain-length of cell wall lipids, such as diacyltrehalose (DAT),

280   polyacyltrehalose (PAT), and sulfolipid-1 (SL-1) (50–53). To understand whether these

281   alterations in cell wall lipids could be responsible for altering RIF efficacy, we compared

282   RIF GR_{50} values in cells grown in cholesterol to those grown in butyrate media

283   supplemented with increasing concentrations of propionate. We observed that GR_{50}

284   values increased up to 8-fold with increasing propionate levels, and the addition of 0.1X

285   propionate, reflecting a 1:10 ratio of propionate to butyrate (weight:weight), mimicked

286   the effect of cholesterol **(Fig5A)**. To more quantitatively associate branched-chain lipid

287   abundance with drug efficacy, we performed relative quantification of the abundance of

288   SL-1 during growth in butyrate, butyrate and propionate, and cholesterol using mass

289   spectrometry. As expected, we found that growth in either propionate or cholesterol

290   increased both the *m/z* range of SL-1 and its total abundance, and the effect of

291   propionate was dose-dependent in the tested range **(Fig5B)**. This dose-dependency

292   allowed us to correlate changes in sulfolipid abundance with changes in rifampicin

293   efficacy. At multiple propionate concentrations, we calculated the GR_{50} for RIF and the

294   total abundance of SL-1. We found a correlation between these values, as 0.003X

295   propionate supplementation had no effect on either SL-1 abundance or RIF GR_{50}, and

296   0.1X increased both values **(Fig5C)**. These findings implied that the propionyl-CoA

297   derived from cholesterol alters rifampicin efficacy through modification of mycobacterial

298   surface lipids.

299

300   The different branched chain lipid species of *Mtb* are produced by distinct biosynthetic

301   pathways, and inhibiting the synthesis of one lipid can produce a compensatory

302   increase in others (52). Therefore, to assess whether increased lipid abundance was

303   causally related to RIF efficacy, we employed an *Mtb* mutant lacking the PhoPR

304   regulatory system, which is required for the synthesis of multiple branched chain lipid

305   species (54–56). In contrast to wild type *Mtb,* a ∆*phoPR* deletion mutant showed little

306   change in rifampicin efficacy with propionate supplementation or cholesterol compared

307   to butyrate growth conditions, and possessed significantly decreased sulfolipid levels

308   compared to WT **(Fig6AB)**. Similar to the effects seen with the ∆*phoPR* mutant, cell wall

309   defective hypomorphs (*aftB, hadB, dapE*) also maintained a relatively consistent RIF

310   GR50 in all media conditions, compared to wild type **(Fig6CD)**. These findings suggest

311   that cholesterol catabolism reduces RIF efficacy via a propionyl-CoA driven increase in

312   synthesis of cell surface lipids, and that this effect can be reversed by perturbing the

313   structure of the cell envelope.

314

In vitro CGI predict drug efficacy *in vivo*

316   To determine whether synergies identified *in vitro* predict strategies to accelerate

317   bacterial killing in the lung, we infected C57BL/6J mice via the aerosol route with a

318   pooled culture consisting of 3 barcoded WT strains and a number of select hypomorph

319   mutants. We concentrated on genes that either displayed carbon source-independent

320   synergy with RIF (*rpoB*, *madR*), or mutants that disrupt the peptidoglycan (*dapE, murA*)

321   or arabinogalactan (*aftB*) layer of the cells wall and would be expected to reverse the

322   effect of host-derived cholesterol catabolism **(Fig3AB, Fig4BC, S.Fig1)**. To ensure that

323   the animals were treated with a relevant dose of antibiotic, we measured the plasma

324   concentration of RIF in mice and adjusted the dosing to match the 24-hour exposure

325   observed during clinical TB therapy **(Fig7A)** (57). The mice were fed doxycycline chow

326   starting 3 days before infection to repress *sspB* expression in the mutants upon

327   infection, and allow them to grow normally. At 3 weeks post-infection, doxycycline was

328   withdrawn to initiate protein degradation, and two weeks of RIF treatment was

329   administered **(Fig7B)** (58). The antibiotic regimen effectively decreased the total

330   number of lung CFU **(Fig7C)**. Lung homogenates were washed free of RIF and plated

331   on 7H10 plates with supplementation to recover viable clones. The relative abundance

332   of individual mutants was normalized to the average abundance of three barcoded WT

333   strains for each mouse and fitness changes were calculated by comparing to those from

334   untreated mice. Each of the mutants showed significant decrease in abundance in RIF

335   treated animals, relative to wild type. AftB and MurA depletion increased bacterial

336   clearance to the same degree as RpoB depletion. Depleting MadR had an even greater

337   effect, and the abundance of this mutant was reduced below our limit of detection in four

338   out of five animals **(Fig7D)**. DapE depletion mutant was below our limit of detection in

339   both untreated and treated animals. These findings show that CGI identified *in vitro* can

340   accelerate bacterial clearance during infection, and highlight the importance of the

341   environment for defining relevant interactions.

342

343   **Discussion**

344   Optimizing combination therapy is critical to improving TB treatment. While efficient

345   strategies for predicting and quantifying drug-drug interactions under *in vitro* conditions

346   have been developed, the impact of bacterial environment on these interactions has not

347   been determined (27, 28). As a result, it remains unclear how well these *in vitro* data

348   predict the effects of combination therapy in the infection environment. In this study, we

349   modeled drug-drug interactions using a newly developed genetic hypomorph library to

350   assess the impact of bacterial carbon metabolism on CGI. This work revealed that

351   synergies with distinct drugs are differentially sensitive to the environment, suggesting

352   tailored approaches to optimization.

353

354   While global analysis of our chemical-genetic-environmental dataset suggested that

355   drug mechanism and environment both play critical roles in shaping chemical-genetic

356   interactions, all drugs were not equally affected by condition. In particular, the individual

357   effect of the fluoroquinolone, MOX, was unaffected by carbon source, and this relative

358   indifference to the environment was also observed for CGI with MOX. These

359   observations contrast with RIF and INH, where carbon source plays an important role in

360   determining the MIC of the drug alone, as well as shaping chemical-genetic interaction

361   profiles. While we can only speculate on the mechanistic basis for these differences

362   between drugs, we found that the cholesterol-dependent decrease in RIF sensitivity is

363   due to the profound effect of carbon source on cell envelope structure that is likely to

364   alter RIF penetration. Similarly, the activation of the prodrug, INH, is affected by the

365   redox state of the cell (59), another process that is impacted by carbon catabolism. In

366   contrast, MOX is not a prodrug and we speculate that it may not be limited by cellular

367   penetration as strongly as RIF. More practically, these observations suggest that drug-

368   drug interactions with MOX may be particularly robust to changes in condition, and

369   therefore may translate well between *in vitro* and *in vivo* conditions.

370

371   While RIF synergies were complex and condition-dependent compared to MOX, we

372   found that the cholesterol-specific effects translate well to the infection environment and

373   may be particularly relevant to treatment. As reduced RIF exposure limits the efficacy of

374   this critical component of our standard regimen, even small increases in MIC during

375   infection could have a significant effect on bacterial killing. A number of observations

376   indicate that RIF efficacy is limited by similar mechanisms *in vivo* and in cholesterol-

377   containing media. Firstly, the increase in branched-chain lipid abundance that is

378   associated with reducing RIF efficacy in cholesterol- or propionate-containing media has

379   also been observed during infection, where similar carbon sources are utilized (16, 52).

380   Furthermore, genetic perturbation of the same cell wall synthetic enzymes sensitized

381   Mtb to RIF in both conditions. This effect may underlie the increased cell-associated RIF

382   upon simultaneous INH and ethambutol treatment *in vitro* (60). While the importance of

383   cell wall architecture and cell envelope lipid production suggests that cellular

384   permeability to RIF may be altered during growth on cholesterol, we note that lipid

385   synthesis also has important effects on central carbon metabolic pathways that could

386   influence antibiotic susceptibility (15). Additional enzymes identified in this study may

387   also be attractive targets for further drug development, such as AftB, a

388   arabinofuranosyltransferase distinct from EmbA and EmbB that are targets of

389   ethambutol (46). Similarly, enzymes in the DAP (diaminopimelic acid) biosynthesis

390   pathway produce precursors for the synthesis of peptidoglycan and lysine (61), and the

391   loss of either sensitizes the cell to RIF.

392

393   Using a chemical-genetic system, we determined that cellular environments can have a

394   profound effect on drug-drug interactions, and that even the use of relatively simple *in*

395   *vitro* culture conditions can identify synergies that are relevant during infection. These

396   studies provide a tractable system that can incorporate more complex culture systems,

397   or even cellular models, to identify additional *in vivo*-relevant synergies. Expanding this

398   CGI atlas promises to elucidate the processes limiting drug efficacy during infection and

399   guide drug development and regiment optimization efforts.

400

401   **Material and methods**

402   **Bacterial cultures**

403   *M. tuberculosis* (H37Rv) cells were cultured in Middlebrook 7H9 medium supplemented

404   with 10% oleic acid-albumin-dextrose-catalase (OADC), 0.5% glycerol, and 0.05%

405   Tween-80, or in minimal medium supplemented with 0.1% Tyloxapol and variable levels

406   of glycerol, acetate, butyrate, propionate, or cholesterol up to 0.1%. Minimal medium

407   was made as previously described but with ferric chloride (100uM) replacing ferric

408   ammonium citrate (50).

409   Cells were also cultured on 7H10 agar medium supplemented with 10% OADC and

410   0.5% glycerol. Streptomycin (20ug/mL) was supplemented when necessary.

411   Anhydrotetracycline (ATC, 500ng/mL) was supplemented periodically until cultures

412   reach exponential growth. ATC was removed from cultures prior to antibiotic growth

413   inhibition assays by washing in PBS supplemented with 0.1% Tyloxapol. *ΔphoPR*

414   mutant was generated as described previously (62).

415

416   **Multiplexed library screening**

417   Library pools of hypomorph mutants were prepared as described previously (32). Pools

418   were grown in minimal medium with 0.1% glycerol, 0.1% acetate, or 0.1% cholesterol

419   on 96-well plates for 2 weeks. Isoniazid and moxifloxacin were used at 1ug/mL and

420   rifampicin was used at 0.062 ug/mL. Antibiotics were subsequently serially diluted in a

421   2-fold manner. An untreated growth condition was included for each study. Samples

422   were inoculated at OD600 0.05 and growth was monitored using OD600. Upon

423   completion, 96-well plates were heat-inactivated at 85 degrees for 2 hours. Barcodes

424   were PCR amplified as described previously (32). Individual libraries were mixed with

425   1:1 20% DMSO and heated for 10 minutes at 98 degrees prior to PCR reaction.

426   Amplified barcodes were purified using SPRI-based purification methods and

427   sequenced using Next-generation sequencing methods. Sequence alignment and

428   analysis were conducted using Bowtie software package with index mismatch set to 2

429   bases and barcode mismatch set to 1 base. Relative abundance of every mutant was

430   calculated as mean ratio of barcode abundance of mutant relative to total barcode

431   abundance of library. Log2FC of a mutant was calculated as the log2 of the ratio of the

432   mean relative abundances in a given antibiotic condition relative to its untreated control.

433   Hierarchical clustering and principal component analysis were conducted using ClustVis

434   (63). Hierarchical clustering was applied to vectors of Log2FC of each gene across all

435   conditions. PCA was performed on relative abundances across all conditions. Statistical

436   significance was determined by unpaired *t*-test with Benjamini-Hochberg multiple testing

437   correction.

438

439   **Antibiotic growth inhibition assay**

440   *Mtb* cells were grown in minimal medium with 0.1% glycerol, 0.01% acetate, 0.01%

441   butyrate, 0.01% propionate, or 0.01% cholesterol on 96-well plates. Isoniazid and

442   moxifloxacin were used at 1ug/ml and rifampicin was used at 0.062 ug/mL. Antibiotics

443   were subsequently serially diluted in a 2-fold manner. Untreated condition was included

444   for each study. Cells were inoculated at OD600 0.05 and growth was monitored using

445   OD600. Antibiotic efficacy was determined using growth rate inhibition as done

446   previously (24). The exponential growth constant (k) value was determined for all

447   conditions. The k-value of each antibiotic concentration was normalized to the k-value of

448   the no-drug control. The GR_{50} value was defined as the concentration of antibiotic that

449   resulted in 50% decrease in growth rate. L-lysine (Sigma) was added to growth

450   conditions to final concentration of 3mM.

451

452   **Lipid extraction and mass spectrometry**

453   *Mtb* cells were grown in minimal medium with 0.01% butyrate, propionate or cholesterol.

454   Cells were inoculated at OD600 0.1 and grown to final OD600 of 0.7. Cells were

455   pelleted and heat-inactivated at 85 degrees for 45 minutes. Cells were washed in 10%

456   glycerol to remove residual detergents from growth media. Lipid extraction was

457   conducted with methyl tert-butyl ether (MTBE) as described previously (64). 1.5mL

458   methanol and 5mL MTBE were mixed with the cell pellet and placed into a glass tube

459   with a Teflon-lined cap. The mixture was incubated at room temperature for 5 hours

460   while shaking. Phase-separation was achieved by adding 0.75mL water to the tubes,

461   incubating for 10 minutes at room temperature, then centrifuging at 1000g for 10

462   minutes. The 2.5mL of the top phase was collected and transferred to a fresh glass tube

463   with Teflon-lined cap. Samples were dried using a nitrogen evaporator and stored in -20

464   degrees prior to injection to mass spectrometer. After evaporation of MTBE, 300 µL of

465   2:1 methanol:chloroform was added to each tube followed by vigorous vortex.

466   Solubilized lipids were then transferred to a new, pre-weighed tube, dried using a

467   nitrogen evaporator, and then tubes were re-weighed to determine the lipid mass in

468   each sample. Then 1.5 µL of 100 ng/µL N-omega-CD_3-octadecanoyl

469   monosialoganglioside GM_2 (Matreya, State College, PA) was added to each sample for

470   normalization and samples were reconstituted in 300 µL of 2:1 methanol: chloroform for

471   mass spectrometry analysis.

472   Samples were analyzed by direct infusion on a syringe pump to an Orbitrap Velos Pro

473   (Thermo Fisher Scientific, Waltham, MA) mass spectrometer operating in the negative

474   electrospray ionization mode. Mass spectra were acquired at a flow rate of 10 µL/min

475   for 2 minutes in two different mass ranges, *m/z* 200-2000 and *m/z* 300-3000, acquiring

476   two replicates for each range using a resolution of 30,000 (*m/z* 200), an AGC target

477   population of $5e^5$ and a maximum ion injection time of 100 ms. Data were analyzed in

478   Xcalibur 2.2 (Thermo Scientific). Briefly, mass spectra were averaged over the entire

479   acquisition range (0-2 minutes), producing one averaged spectrum for each analysis.

480   Peak lists were exported in Excel and intensity data was normalized to the intensity of

481   the GM2 ganglioside spike.

482

483   **Plasma pharmacokinetic analysis**

484   C57BL/6J mice were purchased from Jackson Laboratories. Housing and

485   experimentation were done in accordance with the guidelines set by the Department of

486   Animal Medicine of University of Massachusetts Medical School and Institutional Animal

487   Care and Use Committee and adhered to the laws of the United States and regulations

488   of the Department of Agriculture. Eight- to 12-week mice were administered 0.1g/L RIF

489   through drinking water for three days. Blood was collected during a 12-hour period 24

490   hours post RIF administration, kept on ice, centrifuged at approximately 2500 x g for 5

491   minutes. After centrifugation, plasma was collected and stored at -80°C until analysis.

492   Neat 1 mg/mL DMSO stocks for RIF were serial diluted in 50/50 acetonitrile/water to

493   create neat spiking stocks. Standards and quality control (QC) samples were created by

494   adding 10 µL of spiking stock to 90 µL of drug free plasma. Ten microliters of control,

495   standard, QC, or study sample were added to 100 µL of acetonitrile/methanol 50/50

496   protein precipitation solvent containing 20 ng/mL RIF-d8. Extracts were vortexed for 5

497   minutes and centrifuged at 4000 RPM for 5 minutes. 100 µL of supernatant was

498   combined with 5 µL of 75 mg/mL ascorbic acid to stabilize RIF. 100 µL of mixture was

499   combined with 100 µL of Milli-Q water prior to HPLC-MS/MS analysis. Mouse control

500   plasma (K2EDTA) was sourced from Bioreclamation. Mouse control lungs were

501   collected in house. RIF was sourced from Sigma Aldrich and RIF-d8 was purchased

502   from Toronto Research Chemicals.

503   LC-MS/MS analysis was performed on a Sciex Applied Biosystems Qtrap 6500+ triple-

504   quadrupole mass spectrometer coupled to a Shimadzu Nexera X2 UHPLC system to

505   quantify each drug in plasma. Chromatography was performed on a Agilent SB-C8

506   (2.1x30 mm; particle size, 3.5 µm) using a reverse phase gradient. Milli-Q deionized

507   water with 0.1% formic acid was used for the aqueous mobile phase and 0.1% formic

508   acid in acetonitrile for the organic mobile phase. Multiple-reaction monitoring of

509   precursor/product transitions in electrospray positive-ionization mode was used to

510   quantify the analytes. Sample analysis was accepted if the concentrations of the quality

511   control samples were within 20% of the nominal concentration. The compounds were

512   ionized using ESI positive mode ionization and monitored using masses RIF

513   (823.50/791.60) and RIF-d8 (831.50/799.60). Data processing was performed using

514   Analyst software (version 1.6.2; Applied Biosystems Sciex).

515

516   ***In vivo* antibiotic susceptibility**

517   C57BL/6J mice were purchased from Jackson Laboratories. Housing and

518   experimentation were done in accordance with the guidelines set by the Department of

519   Animal Medicine of University of Massachusetts Medical School and Institutional Animal

520   Care and Use Committee and adhered to the laws of the United States and regulations

521   of the Department of Agriculture. Eight- to 12-week mice were infected with pools of

522   strains at equal ratios through the aerosol route (500 to 1000 CFU/mouse). Mice were

523   fed doxycycline-containing chow (Purina 5001 with 2000 ppm doxycycline, Research

524   Diets C11300-2000i) starting 3 days pre-infection to 21 days post-infection. At 21 days

525   post-infection, 0.1g/L rifampicin was administered through drinking water for 14 days. At

526   35 days post-infection, mice were sacrificed, spleen and lungs were isolated and

527   homogenized, and CFU was determined by plating dilutions on 7H10 agar with 50ug/mL

528   streptomycin and 500ng/mL ATC. For library recovery, approximately 1 million CFU per

529   mouse were plated on 7H10 agar with 50ug/mL streptomycin and 500ng/ml ATC.

530   Genomic DNA was extracted and normalized as done previously (34) and sequenced

531   using multiplex PCR methods. Sequence alignment and analysis were conducted using

532   Bowtie software package as described above. Relative abundance of every mutant was

533   calculated as mean ratio of barcode abundance of mutant relative to the average

534   barcode abundance of three barcoded H37Rv strains. Log2FC of a mutant was

535   calculated as the log2 of the ratio of the mean relative abundances of rifampicin treated

536   mice relative to the untreated mice. Statistical significance was determined by unpaired
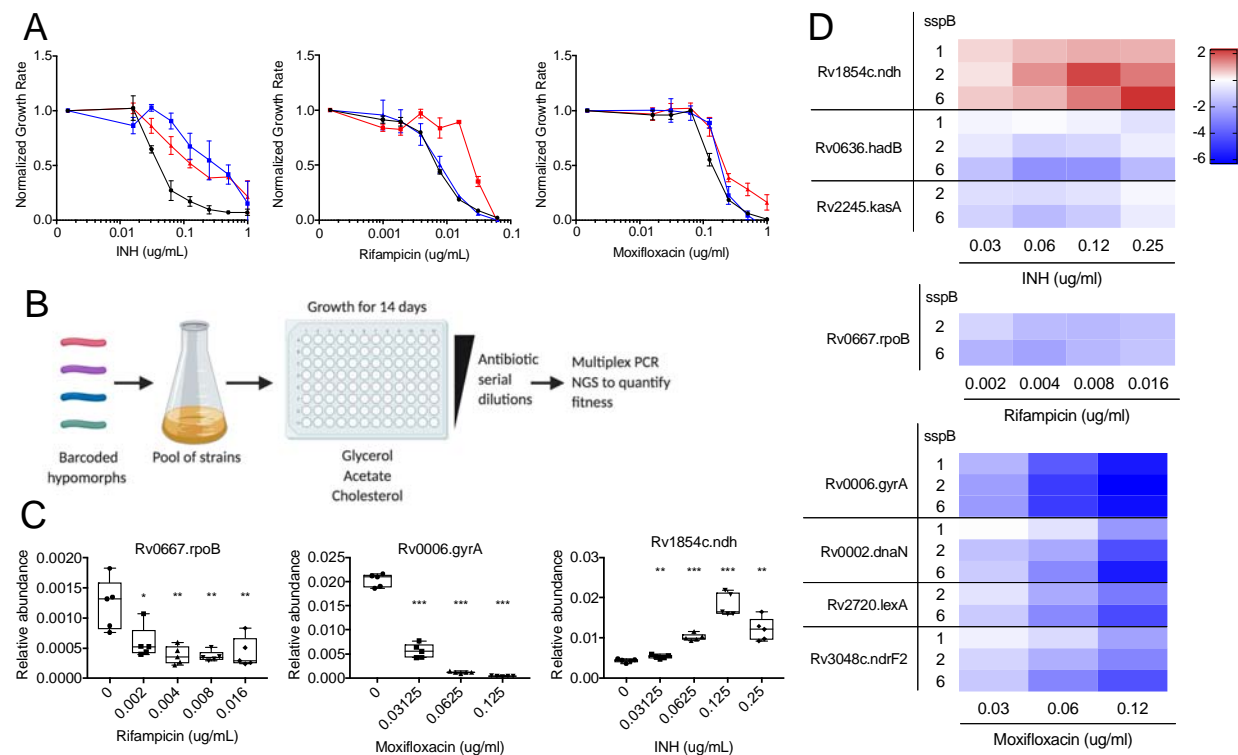
537   *t*-test.

538

539

540

Figure 1. Genetic strategy to define essential bacterial functions that alter drug efficacy *in vitro*. (A) Normalized growth inhibition of WT *Mtb* across increasing concentrations of INH, RIF and MOX in minimal media with glycerol (black), acetate (blue) and cholesterol (red) as sole carbon sources. Results shown as means from 3 biological replicates with standard deviations. **(B)** Barcoded hypomorph mutants were pooled and grown in 96-well plates containing minimal media with glycerol, acetate or cholesterol as the sole carbon source for 14 days. Antibiotics were added to individual wells as well as untreated controls. Chromosomal barcodes were PCR amplified and pooled for Illumina Next Generation Sequencing (NGS). Barcodes were analyzed to quantify changes in fitness of individual strains from different conditions. **(C)** Boxplot representing changes in relative abundances of *rpoB*, *gyrA* and *ndh* mutants during RIF, MOX and INH treatment respectively. Data represents 5 biological replicates. Significance was calculated using unpaired t-test and compared to untreated conditions,

554   *p<0.05, **p<0.01, ***p<0.001. **(D)** Heat map representing changes in fitness of

555   individual mutants, shown as Log2 fold change, during INH, RIF and MOX treatment in

556   glycerol growth conditions. Mutants were chosen from previous association with

557   respective antibiotic. sspB numbers denote *sspB* expression level of mutant. Results

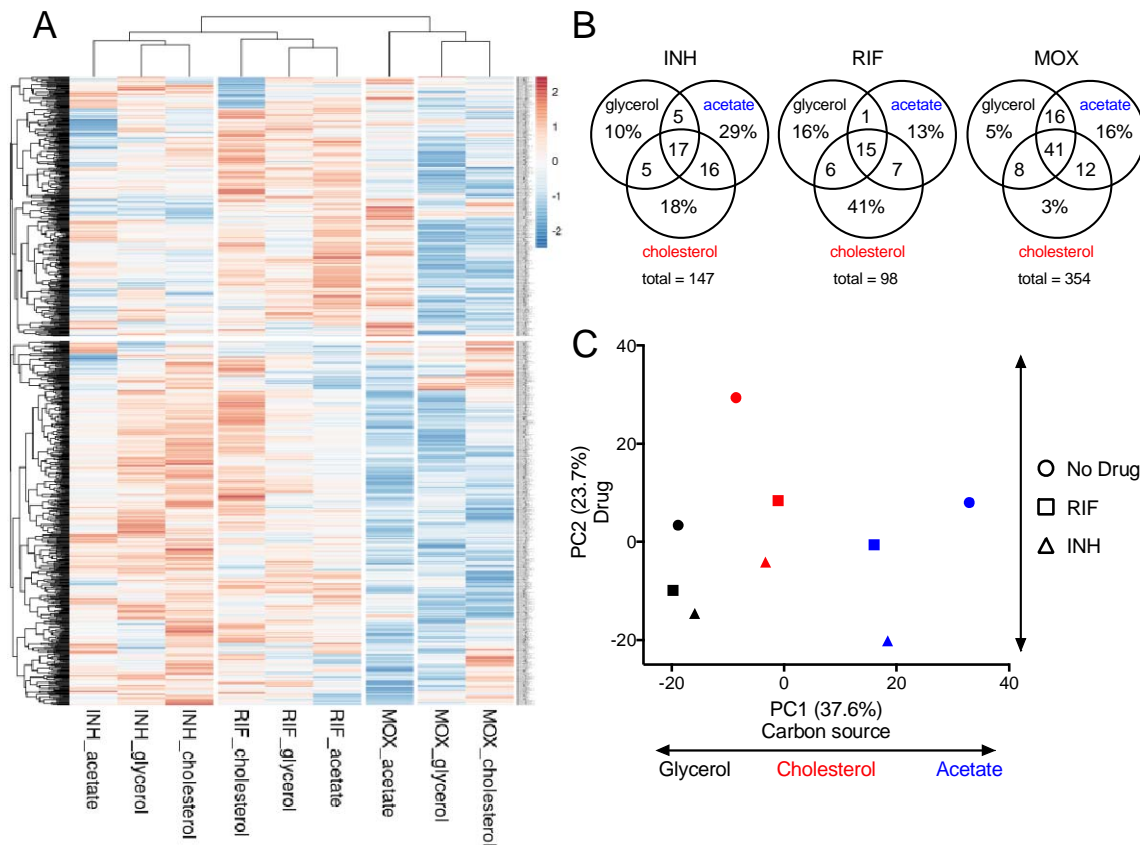558   shown as means from 5 biological replicates.

559

560

Figure 2. Carbon sources mediate antibiotic-genetic interactions of essential bacterial functions. (A) Heat map of hypomorph mutants shown as Log2 fold change of 0.65X GR_{50} of INH, RIF and MOX against untreated controls. Results shown as means from 5 biological replicates. Each antibiotic (INH, RIF and MOX) in single carbon source (glycerol, acetate and cholesterol) conditions were compared using hierarchical clustering methods. **(B)** Venn diagrams showing the total number of genes with log2FC > -1 and $p<0.05$ at 0.65X GR_{50} of INH, RIF and MOX, and the % of genes associated with specific conditions. **(C)** Relative abundance datasets of the hypomorph libraries from glycerol (black), acetate (blue) and cholesterol (red) growth conditions with 0.65X GR_{50} INH (triangle) and RIF (square) treatment as well as untreated controls (circle)

572   were examined using principal component analysis. Units shown on axes are arbitrary
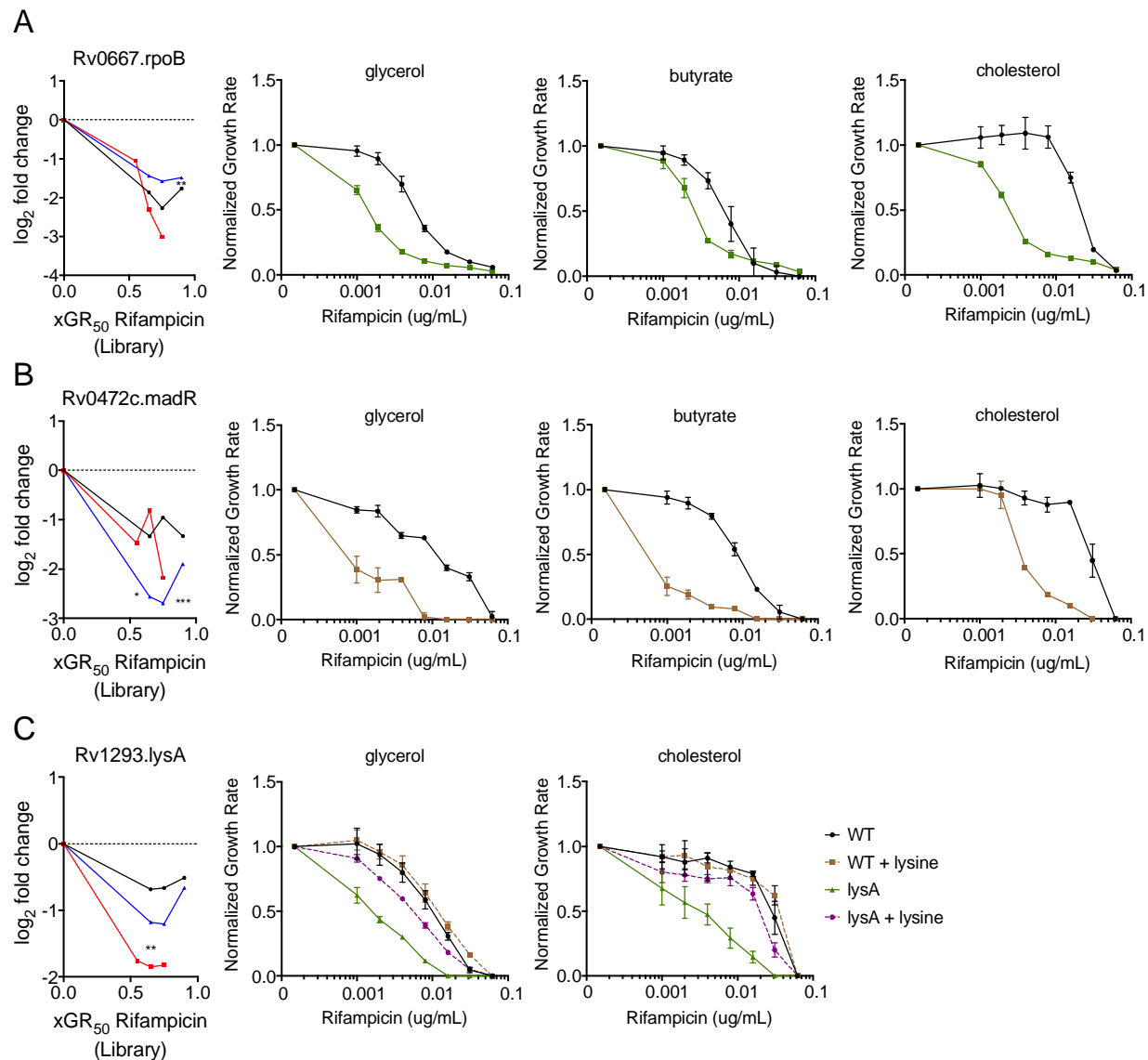
573   values in principal component space.

574

575

Figure 3. Condition-independent chemical-genetic synergies can be reproduced with individual mutants. (A) RpoB depletion shows decreased fitness compared to the library over increasing concentrations of RIF for glycerol (black), acetate (blue) and cholesterol (red). Normalized growth inhibition assay shows *rpoB* hypomorph mutant (green) has decreased RIF MIC compared to WT (black) across multiple carbon conditions. **(B)** MadR depletion shows decreased fitness compared to the library over increasing concentrations of rifampicin for glycerol (black), acetate (blue) and

583   cholesterol (red). Normalized growth inhibition assay shows *madR* hypomorph mutant

584   (brown) has decreased RIF MIC compared to WT (black) across multiple carbon

585   conditions. **(C)** LysA depletion shows decreased fitness compared to the library over

586   increasing concentrations of rifampicin for glycerol (black), acetate (blue) and

587   cholesterol (red). Normalized growth inhibition assay shows *lysA* hypomorph mutant

588   (green) has decreased RIF MIC compared to WT (black), which can be reversed by

589   3mM lysine supplementation (purple). Library results are shown as means from 5

590   biological replicates, and significance was calculated using unpaired t-test with

591   Benjamini-Hochberg multiple testing correction, *$q<0.05$, **$q<0.01$, ***$q<0.001$.

592   Normalized growth inhibition results are shown as means from 3 biological replicates

593   with standard deviations.
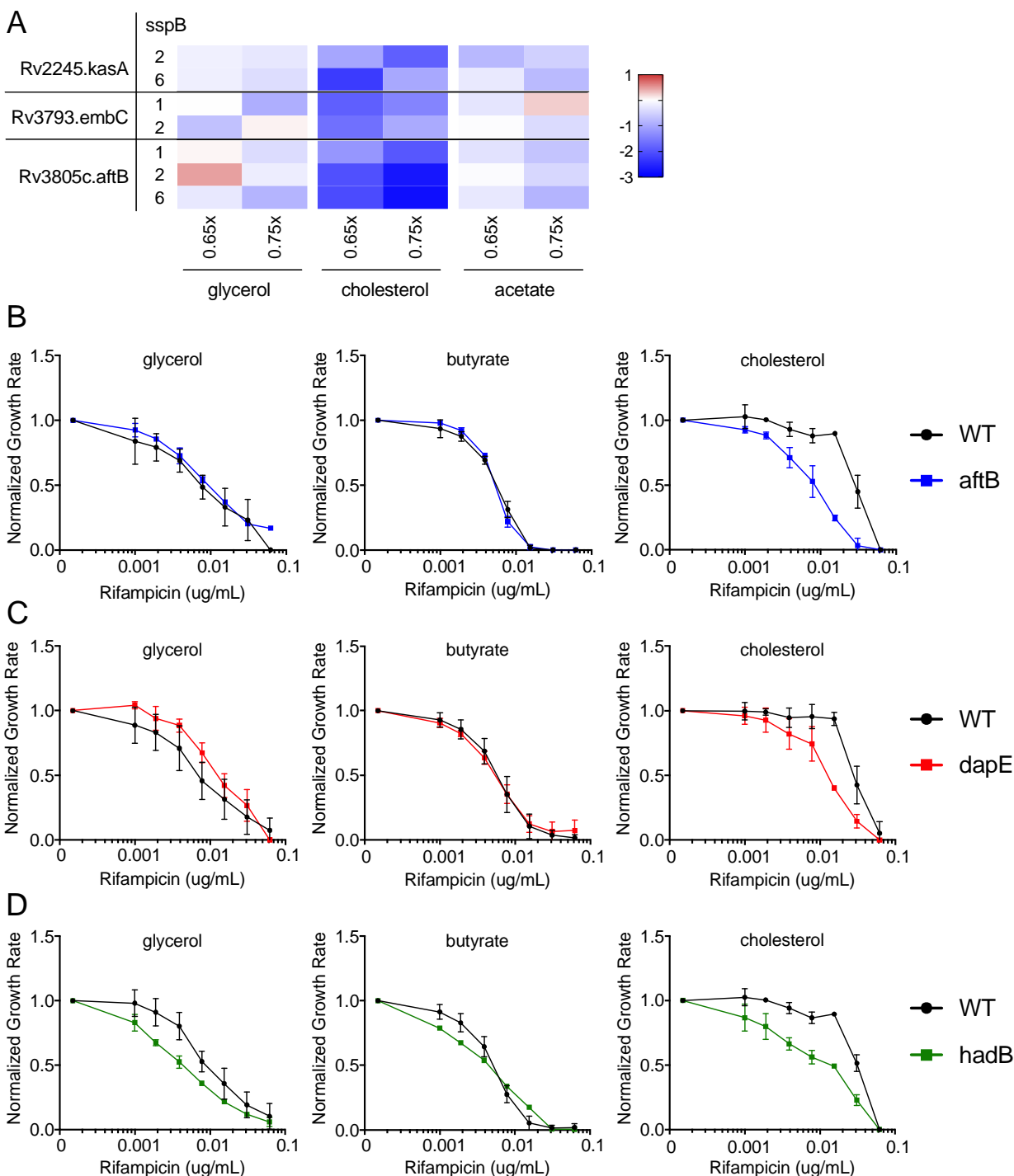
594

595

596

Figure 4. Cell-wall biosynthesis hypomorph mutants show altered RIF efficacy

during cholesterol growth conditions. (A) Heat map showing hypomorph mutants of

select mycobacterial cell-wall biosynthesis genes and pathways with significant changes

600   in fitness during cholesterol growth, shown as Log2 fold change at 0.65X and 0.75X

601   GR_{50} of RIF against untreated controls. Results shown as means from 5 biological

602   replicates. Classification of mutants was done using Mycobrowser. **(B-D)** Normalized

603   growth inhibition of WT and select mutants across increasing concentrations of RIF in

604   minimal media with sole carbon sources. Depletion of AftB (blue), DapE (red) and HadB

605   (green) show decreased RIF MIC compared to WT (black) only during cholesterol

606   growth conditions. Results shown as means from 3 biological replicates with standard
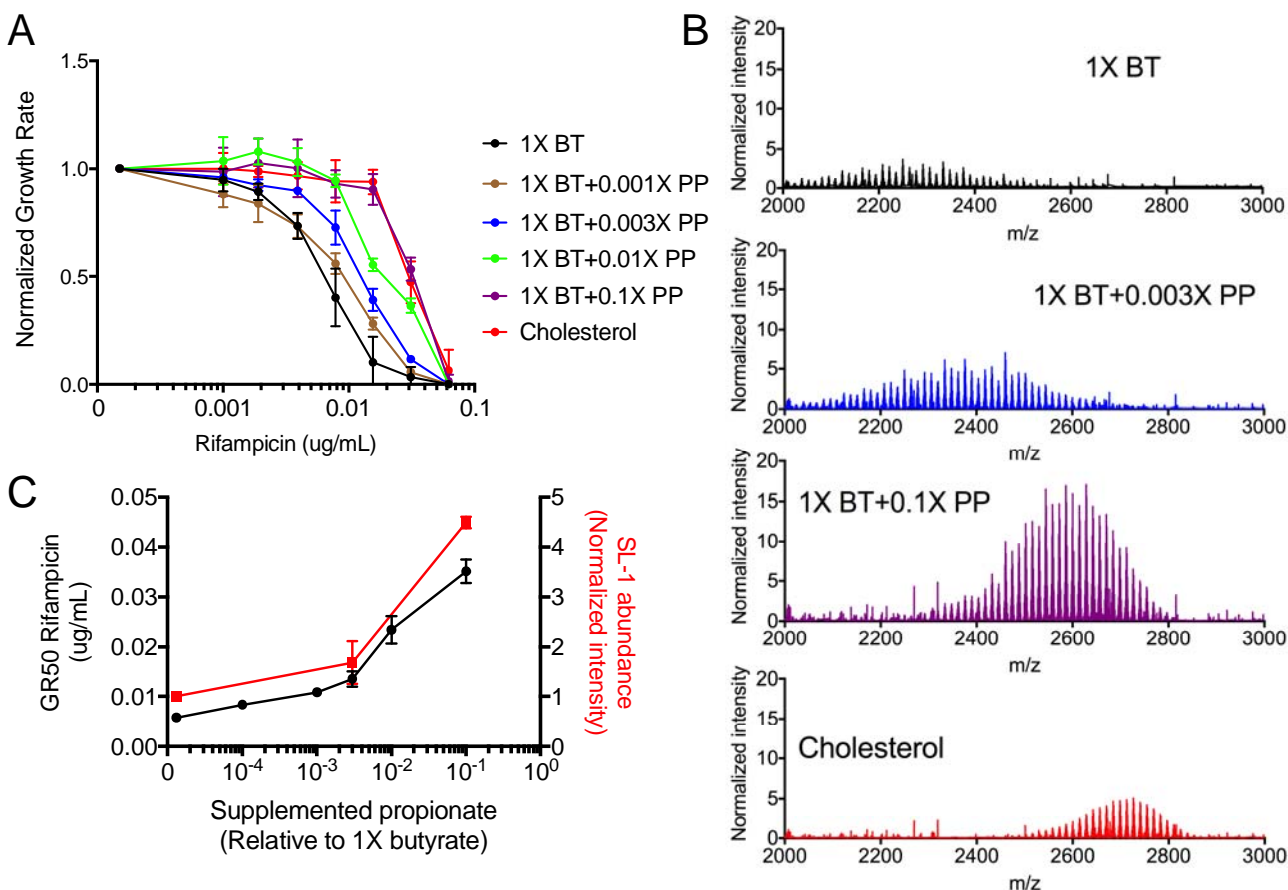
607   deviations.

608

609

Figure 5. Propionate and cholesterol catabolism decreases RIF efficacy in

correlation with increased branched chain lipid length and abundance. (A)

Normalized growth inhibition of WT across increasing concentrations of RIF in minimal

media with 1X butyrate (BT) and corresponding propionate (PP) supplementations as

well as cholesterol. Results shown as means from 3 biological replicates with standard

deviations. **(B)** Normalized mass spectra of extracted sulfolipids from WT grown in

minimal media with 1X butyrate (BT) and corresponding propionate (PP)

supplementations as well as cholesterol. MS spectra intensities were normalized using

GM2 ganglioside internal standard and cell density. Results shown as representative

from 2 biological and 2 technical replicates. **(C)** Plotted GR_{50} values (black) and relative

622   sulfolipid abundances (red) across increasing propionate levels. Relative sulfolipid

623   abundances were determined by the combined normalized mass spectra intensities

624   from *m/z* 2000-2800 for each growth condition. Results shown as means with standard
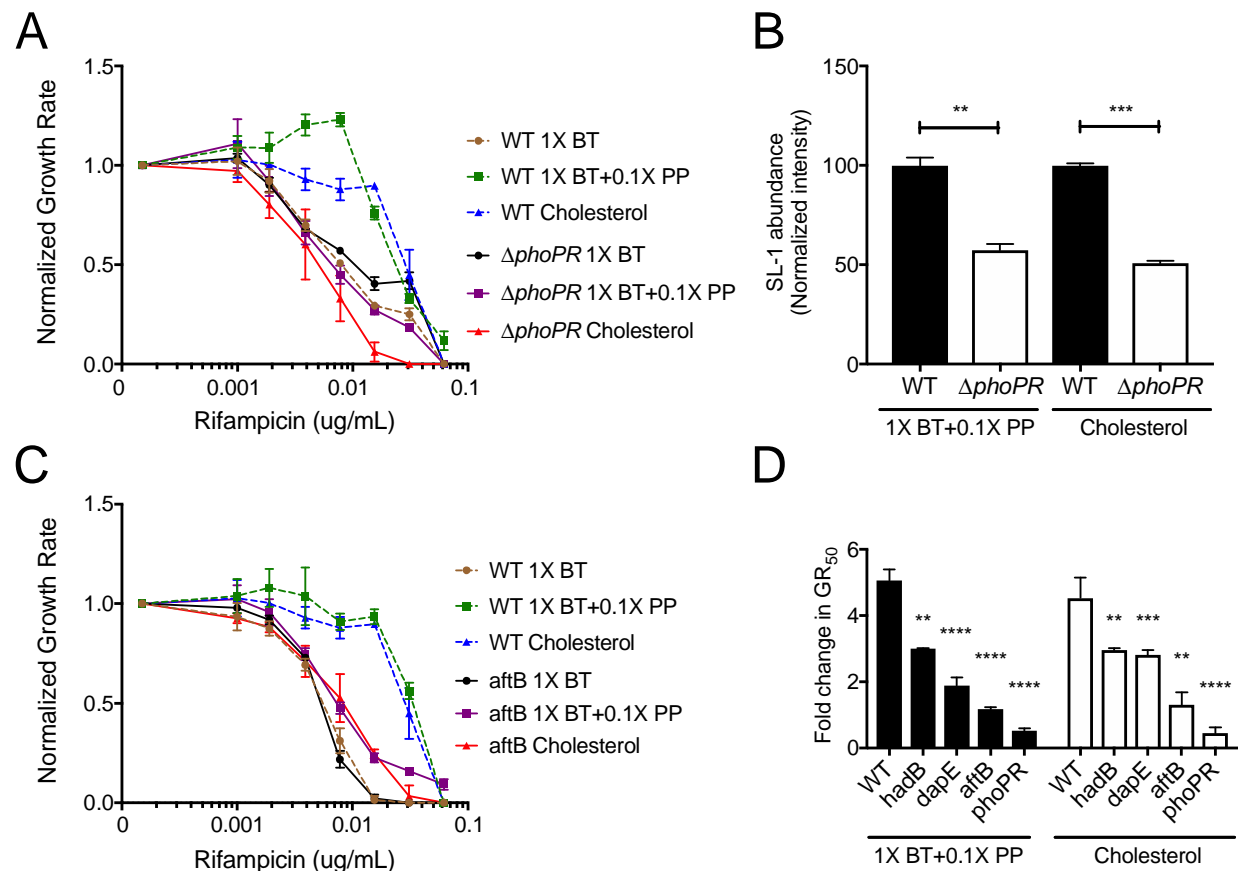
625   deviations.

626

627

628

Figure 6. Disruption of the cell envelope reverses propionate and cholesterol catabolism dependent decrease in RIF efficacy. (A) Normalized growth inhibition of Δ*phoPR* mutant across increasing concentrations of RIF in minimal media compared to WT. Results shown as means from 3 biological replicates. **(B)** Relative sulfolipid abundances of WT and Δ*phoPR* mutant grown in minimal media with 1X butyrate and 0.1X propionate (1X BT+0.1X PP), and cholesterol. Relative sulfolipid abundances were determined by the combined normalized mass spectra intensities from *m/z* 2000-2800 for each growth condition. MS spectra intensities were normalized using GM2 ganglioside internal standard and cell density. Results shown as means with standard deviations from 2 biological and 2 technical replicates. Significance was calculated using unpaired t-test, **p*<0.05, ***p*<0.01. **(C)** Normalized growth inhibition of *aftB* mutant

641   across increasing concentrations of RIF in minimal media compared to WT. Results

642   shown as means from 3 biological replicates. **(D)** Calculated fold change in GR_{50} values

643   of 1X butyrate and 0.1X propionate (1X BT+0.1X PP) and cholesterol conditions against

644   1X butyrate alone for WT and mutant strains. Significance was calculated using

645   unpaired t-test, **$p<0.01$, ***$p<0.001$, ****$p<0.0001$.
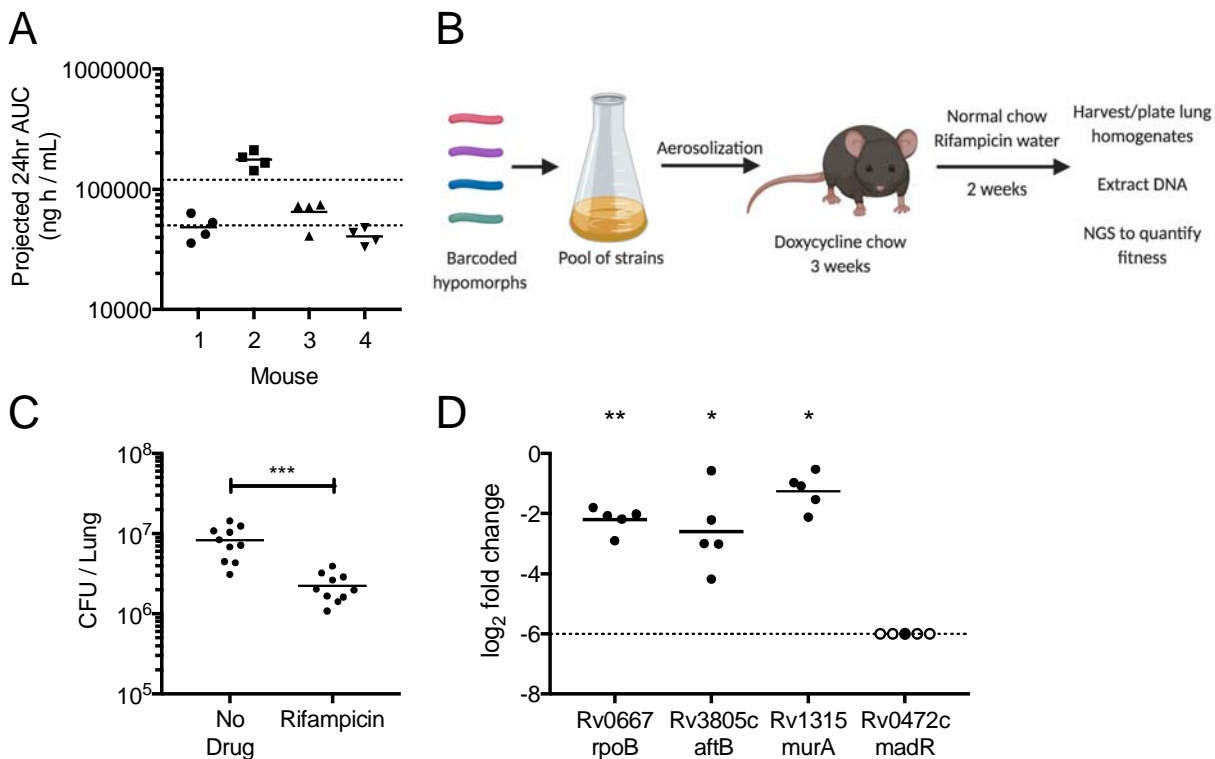
646

Figure 7. Essential bacterial functions that alter drug efficacy *in vivo*. (A) RIF

plasma concentrations were measured in mice over 12-hour period 24 hours post RIF

administration (0.1g/L). Results shown as Area Under the Concentration (AUC) time

profile. Dotted lines indicate RIF plasma range observed during clinical TB therapy (57).

(B) C57BL/6J mice were infected through the aerosol route with a pooled culture of

individual hypomorph mutants and barcoded WT strains. Mice were fed doxycycline

chow starting 3 days before infection to 3 weeks post infection. Mice were subsequently

switched to normal chow and water with or without RIF (0.1g/L) for 2 additional weeks.
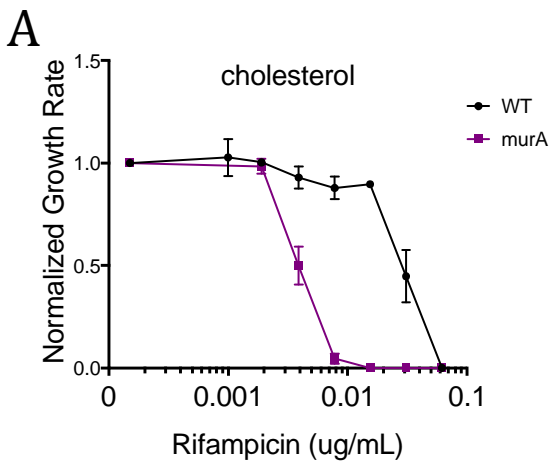
Lungs were harvested, homogenized and plated for *Mtb* outgrowth. Upon DNA

extraction of grown colonies, chromosomal barcodes were PCR amplified and pooled

for Illumina Next Generation Sequencing (NGS). Barcode abundances of individual

mutants were normalized to WT strains and analyzed to quantify changes in fitness

660   during RIF treatment. **(C)** RIF treated mice show significant decrease in *Mtb* CFU in

661   lungs compared to untreated controls. Each dot represents a single mouse. Significance

662   was calculated using unpaired t-test, ***p<0.001. **(D)** Depletion of RpoB, AftB and MurA

663   show significant decrease in fitness, shown as Log2 fold change, during rifampicin

664   treatment compared to untreated controls. Each dot represents a single mouse and

665   empty dot indicates that the relative abundance was below the limit of detection (Dotted

666   line). Significance was calculated using unpaired t-test, *p<0.05, **p<0.01

667

668

669

Supplementary Figure 1. MurA hypomorph mutant shows altered RIF efficacy during cholesterol growth conditions. (A) Normalized growth inhibition of WT and MurA hypomorph mutant across increasing concentrations of RIF in minimal media with cholesterol as the sole carbon source. Depletion of MurA (purple) show decreased RIF MIC compared to WT (black) during cholesterol growth conditions. Results shown as means from 3 biological replicates with standard deviations.

677 **Acknowledgements**

686   1. ,   Streptomycin Treatment of Pulmonary Tuberculosis. *Br. Med. J.* **2**, 769–782 (1948).

687   2.   W. Fox, D. Mitchison, Short-course chemotherapy for pulmonarytuberculosis. *Am Rev*
688   *Respir Dis* **111**, 325–353 (1975).

689   3.   World Health Organization, *Guidelines for treatment of tuberculosis, 4th edition* (World
690   Health Organization, 2010).

691   4.   World Health Organization, *Global tuberculosis report 2020.* (World Health
692   Organization, 2020).

693   5.   S. H. Gillespie, *et al.*, Four-Month Moxifloxacin-Based Regimens for Drug-Sensitive
694   Tuberculosis. *http://dx.doi.org/10.1056/NEJMoa1407426* (2014)
695   https:/doi.org/10.1056/NEJMoa1407426 (November 4, 2020).

696   6.   P. Nahid, *et al.*, Treatment of Drug-Resistant Tuberculosis. An Official
697   ATS/CDC/ERS/IDSA Clinical Practice Guideline. *Am. J. Respir. Crit. Care Med.* **200**, e93–
698   e142 (2019).

699   7.   J. E. Gomez, J. D. McKinney, M. tuberculosis persistence, latency, and drug tolerance.
700   *Tuberculosis* **84**, 29–44 (2004).

701   8.   A. A. Ordonez, *et al.*, Dynamic imaging in patients with tuberculosis reveals
702   heterogeneous drug exposures in pulmonary lesions. *Nat. Med.* **26**, 529–534 (2020).

703   9.   M. C. Kjellsson, *et al.*, Pharmacokinetic Evaluation of the Penetration of
704   Antituberculosis Agents in Rabbit Pulmonary Lesions. *Antimicrob. Agents Chemother.*
705   **56**, 446–457 (2012).

706   10.   R. J. Svensson, *et al.*, Greater Early Bactericidal Activity at Higher Rifampicin Doses
707   Revealed by Modeling and Clinical Trial Simulations. *J. Infect. Dis.* **218**, 991–999
708   (2018).

709   11.   M. J. Boeree, *et al.*, High-dose rifampicin, moxifloxacin, and SQ109 for treating
710   tuberculosis: a multi-arm, multi-stage randomised controlled trial. *Lancet Infect. Dis.*
711   **17**, 39–49 (2017).

712   12.   S.-H. Baek, A. H. Li, C. M. Sassetti, Metabolic regulation of mycobacterial growth and
713   antibiotic sensitivity. *PLoS Biol.* **9**, e1001065 (2011).

714   13.   K. N. Adams, *et al.*, Drug Tolerance in Replicating Mycobacteria Mediated by a
715   Macrophage-Induced Efflux Mechanism. *Cell* **145**, 39–53 (2011).

716   14.   Y. Liu, *et al.*, Immune activation of the host cell induces drug tolerance in
717   Mycobacterium tuberculosis both in vitro and in vivo. *J. Exp. Med.* **213**, 809–825
718   (2016).

719   15.   R. R. Lovewell, C. M. Sassetti, B. C. VanderVen, Chewing the fat: lipid metabolism and
720   homeostasis during M. tuberculosis infection. *Curr. Opin. Microbiol.* **29**, 30–36 (2016).

721   16.   A. K. Pandey, C. M. Sassetti, Mycobacterial persistence requires the utilization of host
722   cholesterol. *Proc. Natl. Acad. Sci. U. S. A.* **105**, 4376–4380 (2008).

723   17.   A. D. Baughn, K. Y. Rhee, Metabolomics of Central Carbon Metabolism in
724   Mycobacterium tuberculosis. *Microbiol. Spectr.* **2** (2014).

725   18.   D. A. Aguilar-Ayala, *et al.*, Antimicrobial activity against Mycobacterium tuberculosis
726   under in vitro lipid-rich dormancy conditions. *J. Med. Microbiol.* **67**, 282–285 (2018).

727   19.   J. J. Baker, R. B. Abramovitch, Genetic and metabolic regulation of Mycobacterium
728   tuberculosis acid growth arrest. *Sci. Rep.* **8**, 1–16 (2018).

729   20.   S. G. Franzblau, *et al.*, Comprehensive analysis of methods used for the evaluation of
730   compounds against Mycobacterium tuberculosis. *Tuberculosis* **92**, 453–488 (2012).

731   21.   K. Pethe, *et al.*, A chemical genetic screen in Mycobacterium tuberculosis identifies
732   carbon-source-dependent growth inhibitors devoid of in vivo efficacy. *Nat. Commun.* **1**,
733   1–8 (2010).

734   22.   P. Gopal, *et al.*, Pyrazinamide Resistance Is Caused by Two Distinct Mechanisms:
735   Prevention of Coenzyme A Depletion and Loss of Virulence Factor Synthesis. *ACS*
736   *Infect. Dis.* **2**, 616–626 (2016).

737   23.   N. P. Kalia, *et al.*, Carbon metabolism modulates the efficacy of drugs targeting the
738   cytochrome bc1:aa3 in Mycobacterium tuberculosis. *Sci. Rep.* **9** (2019).

739   24.   M. M. Bellerose, *et al.*, Common Variants in the Glycerol Kinase Gene Reduce
740   Tuberculosis Drug Efficacy. *mBio* **10**, e00663-19 (2019).

741   25.   N. D. Hicks, *et al.*, Clinically prevalent mutations in Mycobacterium tuberculosis alter
742   propionate metabolism and mediate multidrug tolerance. *Nat. Microbiol.* **3**, 1032–
743   1042 (2018).

744   26.   G. R. Zimmermann, J. Lehár, C. T. Keith, Multi-target therapeutics: when the whole is
745   greater than the sum of the parts. *Drug Discov. Today* **12**, 34–42 (2007).

746   27.   M. Cokol, N. Kuru, E. Bicak, J. Larkins-Ford, B. B. Aldridge, Efficient measurement and
747   factorization of high-order drug interactions in Mycobacterium tuberculosis. *Sci. Adv.*
748   **3**, e1701881 (2017).

749   28.   S. Ma, *et al.*, Transcriptomic Signatures Predict Regulators of Drug Synergy and Clinical
750   Regimen Efficacy against Tuberculosis. *mBio* **10** (2019).

751   29. J. Pasipanodya, T. Gumbo, An Oracle: Antituberculosis Pharmacokinetics-
752   Pharmacodynamics, Clinical Correlation, and Clinical Trial Simulations To Predict the
753   Future. *Antimicrob. Agents Chemother.* **55**, 24–34 (2011).

754   30. E. Nuermberger, C. Sizemore, K. Romero, D. Hanna, Toward an Evidence-Based
755   Nonclinical Road Map for Evaluating the Efficacy of New Tuberculosis (TB) Drug
756   Regimens: Proceedings of a Critical Path to TB Drug Regimens-National Institute of
757   Allergy and Infectious Diseases In Vivo Pharmacology Workshop for TB Drug
758   Development. *Antimicrob. Agents Chemother.* **60**, 1177–1182 (2016).

759   31. J.-H. Kim, *et al.*, Protein inactivation in mycobacteria by controlled proteolysis and its
760   application to deplete the beta subunit of RNA polymerase. *Nucleic Acids Res.* **39**,
761   2210–2220 (2011).

762   32. E. O. Johnson, *et al.*, Large-scale chemical–genetics yields new M. tuberculosis inhibitor
763   classes. *Nature* **571**, 72–78 (2019).

764   33. J. M. Stokes, A. J. Lopatkin, M. A. Lobritz, J. J. Collins, Bacterial Metabolism and
765   Antibiotic Efficacy. *Cell Metab.* **30**, 251–259 (2019).

766   34. M. M. Bellerose, *et al.*, Distinct Bacterial Pathways Influence the Efficacy of Antibiotics
767   against Mycobacterium tuberculosis. *mSystems* **5** (2020).

768   35. M. Hafner, M. Niepel, M. Chung, P. K. Sorger, Growth rate inhibition metrics correct for
769   confounders in measuring sensitivity to cancer drugs. *Nat. Methods* **13**, 521–527
770   (2016).

771   36. A. S. G. Lee, A. S. M. Teo, S.-Y. Wong, Novel Mutations in ndh in Isoniazid-Resistant
772   Mycobacterium tuberculosis Isolates. *Antimicrob. Agents Chemother.* **45**, 2157–2159
773   (2001).

774   37. J.-H. Kim, *et al.*, A genetic strategy to identify targets for the development of drugs that
775   prevent bacterial persistence. *Proc. Natl. Acad. Sci.* **110**, 19095–19100 (2013).

776   38. J.-R. Wei, *et al.*, Depletion of antibiotic targets has widely varying effects on growth.
777   *Proc. Natl. Acad. Sci.* **108**, 4176–4181 (2011).

778   39. G. Giaever, *et al.*, Genomic profiling of drug sensitivities via induced haploinsufficiency.
779   *Nat. Genet.* **21**, 278–283 (1999).

780   40. E. J. Peterson, *et al.*, Path-seq identifies an essential mycolate remodeling program for
781   mycobacterial host adaptation. *Mol. Syst. Biol.* **15** (2019).

782   41. R. V. der Geize, *et al.*, A gene cluster encoding cholesterol catabolism in a soil
783   actinomycete provides insight into Mycobacterium tuberculosis survival in
784   macrophages. *Proc. Natl. Acad. Sci.* **104**, 1947–1952 (2007).

785 42. A. H. Diacon, *et al.*, Early Bactericidal Activity of High-Dose Rifampin in Patients with
786   Pulmonary Tuberculosis Evidenced by Positive Sputum Smears. *Antimicrob. Agents*
787   *Chemother.* **51**, 2994–2996 (2007).

788 43. E. Chigutsa, *et al.*, Impact of Nonlinear Interactions of Pharmacokinetics and MICs on
789   Sputum Bacillary Kill Rates as a Marker of Sterilizing Effect in Tuberculosis.
790   *Antimicrob. Agents Chemother.* **59**, 38–45 (2015).

791 44. J. G. Pasipanodya, *et al.*, Serum Drug Concentrations Predictive of Pulmonary
792   Tuberculosis Outcomes. *J. Infect. Dis.* **208**, 1464–1473 (2013).

793 45. M. Jankute, J. A. G. Cox, J. Harrison, G. S. Besra, Assembly of the Mycobacterial Cell Wall.
794   *Annu. Rev. Microbiol.* **69**, 405–423 (2015).

795 46. M. Seidel, *et al.*, Identification of a Novel Arabinofuranosyltransferase AftB Involved in
796   a Terminal Step of Cell Wall Arabinan Biosynthesis in Corynebacterianeae, such as
797   Corynebacterium glutamicum and Mycobacterium tuberculosis. *J. Biol. Chem.* **282**,
798   14729–14740 (2007).

799 47. V. Usha, *et al.*, Reconstruction of diaminopimelic acid biosynthesis allows
800   characterisation of Mycobacterium tuberculosis N -succinyl-L,L-diaminopimelic acid
801   desuccinylase. *Sci. Rep.* **6**, 1–10 (2016).

802 48. M. Jankute, *et al.*, Disruption of Mycobacterial AftB Results in Complete Loss of
803   Terminal β(1 ‑ 2) Arabinofuranose Residues of Lipoarabinomannan. *ACS Chem. Biol.*
804   **12**, 183–190 (2017).

805 49. C. Lefebvre, *et al.*, HadD, a novel fatty acid synthase type II protein, is essential for
806   alpha- and epoxy-mycolic acid biosynthesis and mycobacterial fitness. *Sci. Rep.* **8**, 1–15
807   (2018).

808 50. J. E. Griffin, *et al.*, Cholesterol Catabolism by Mycobacterium tuberculosis Requires
809   Transcriptional and Metabolic Adaptations. *Chem. Biol.* **19**, 218–227 (2012).

810 51. M. Jackson, G. Stadthagen, B. Gicquel, Long-chain multiple methyl-branched fatty acid-
811   containing lipids of Mycobacterium tuberculosis: Biosynthesis, transport, regulation
812   and biological activities. *Tuberculosis* **87**, 78–86 (2007).

813 52. M. Jain, *et al.*, Lipidomics reveals control of Mycobacterium tuberculosis virulence
814   lipids via metabolic coupling. *Proc. Natl. Acad. Sci.* **104**, 5133–5138 (2007).

815 53. X. Yang, N. M. Nesbitt, E. Dubnau, I. Smith, N. S. Sampson, Cholesterol Metabolism
816   Increases the Metabolic Pool of Propionate in M. tuberculosis. *Biochemistry* **48**, 3819–
817   3821 (2009).

818   54.   S. B. Walters, *et al.*, The Mycobacterium tuberculosis PhoPR two-component system
819   regulates genes essential for virulence and complex lipid biosynthesis. *Mol. Microbiol.*
820   **60**, 312–330 (2006).

821   55.   J. G. Asensio, *et al.*, The Virulence-associated Two-component PhoP-PhoR System
822   Controls the Biosynthesis of Polyketide-derived Lipids in Mycobacterium tuberculosis.
823   *J. Biol. Chem.* **281**, 1313–1316 (2006).

824   56.   J. J. Baker, B. K. Johnson, R. B. Abramovitch, Slow growth of Mycobacterium
825   tuberculosis at acidic pH is regulated by phoPR and host-associated carbon sources.
826   *Mol. Microbiol.* **94**, 56–69 (2014).

827   57.   K. E. Stott, *et al.*, Pharmacokinetics of rifampicin in adult TB patients and healthy
828   volunteers: a systematic review and meta-analysis. *J. Antimicrob. Chemother.* **73**,
829   2305–2313 (2018).

830   58.   M. Gengenbacher, *et al.*, Tissue Distribution of Doxycycline in Animal Models of
831   Tuberculosis. *Antimicrob. Agents Chemother.* **64** (2020).

832   59.   N. L. Wengenack, H. M. Hoard, F. Rusnak, Isoniazid Oxidation by Mycobacterium
833   tuberculosis KatG: A Role for Superoxide Which Correlates with Isoniazid
834   Susceptibility. *J. Am. Chem. Soc.* **121**, 9748–9749 (1999).

835   60.   M. B. McNeil, S. Chettiar, D. Awasthi, T. Parish, Cell wall inhibitors increase the
836   accumulation of rifampicin in Mycobacterium tuberculosis. *Access Microbiol.* **1** (2019).

837   61.   M. S. Pavelka, W. R. Jacobs, Biosynthesis of diaminopimelate, the precursor of lysine
838   and a component of peptidoglycan, is an essential function of Mycobacterium
839   smegmatis. *J. Bacteriol.* **178**, 6496–6507 (1996).

840   62.   J. Lee, T. Repasy, K. Papavinasasundaram, C. Sassetti, H. Kornfeld, Mycobacterium
841   tuberculosis Induces an Atypical Cell Death Mode to Escape from Infected
842   Macrophages. *PLOS ONE* **6**, e18367 (2011).

843   63.   T. Metsalu, J. Vilo, ClustVis: a web tool for visualizing clustering of multivariate data
844   using Principal Component Analysis and heatmap. *Nucleic Acids Res.* **43**, W566–W570
845   (2015).

846   64.   V. Matyash, G. Liebisch, T. V. Kurzchalia, A. Shevchenko, D. Schwudke, Lipid extraction
847   by methyl-tert-butyl ether for high-throughput lipidomics. *J. Lipid Res.* **49**, 1137–1146
848   (2008).

849